Juan Carlos Labraga

Simulation capability of tropical and extratropical seasonal climate anomalies over South America

Abstract An ensemble of 20 extended integrations of the atmospheric model CSIRO Mark 2, forced with the sea-surface temperature observed during the 1986–1998 period, was performed to analyze the simulation capability of seasonal climate anomalies over South America and adjacent oceanic areas. Variations of the simulation skill within the region and during the experimental period were assessed through standard statistical measures and compared to the signal-to-noise ratio distribution. Before the skill assessment, model systematic errors were thoroughly evaluated. The results confirm that the simulation skill is very high in tropical oceanic areas, and decreases rapidly towards middle and high latitudes. Model performance at mid and high atmospheric levels is substantially better than at low levels. Relatively high simulation capability was found over the Pacific Ocean between the equator and the Antarctic coast, which is coherent with the presence of three relative maximums in the signal-to-noise ratio, similar to the increase of the forced variance found by several authors over much of the Pacific–North American pattern region. Rainfall rate and second-order moments associated with the cyclonic activity and the meridional eddy fluxes of heat and humidity are better simulated in a narrow strip parallel to the SPCZ and extending further southeast into mid latitudes of the continent. The simulation skill noticeably improves during the warm and cold ENSO phases, in correspondence with an intensification of the signal-to-noise ratio, and useful rainfall anomaly simulations can be obtained over the Amazonas and Rio de la Plata river basins.

J. C. Labraga (✉)
Centro Nacional Patagònico - CONICET,
Puerto Madryn, Argentina
E-mail: labraga@cenpat.edu.arv
Tel.: +54-2965-451024
Fax: +54-2965-451543

Introduction

Statistical and numerical models are used routinely to provide forecasts of seasonal-scale climate anomalies of great scientific and social interest. The relative merits of some of these model simulations have been exhaustively compared (Anderson et al. 1999). The atmospheric general circulation models (AGCM) constitute one of the most powerful tools for the study of climate variability and seasonal or longer scale climate forecast. Numerous works published in recent years exemplify the progressive advances achieved on the matters and the challenges foreseen for the near future (Chen and Van den Dool 1997; Déqué 1997; Shukla et al. 2000; Anderson and Ploshay 2000; Chang et al. 2000). A discussion on the main theoretical and practical topics of the climate forecast, and a survey on the status of the acquired knowledge and of the developed capability can be found in the revision carried on by Goddard et al. (2001).

Different approaches to the mathematical problem of climate forecast can be found in literature. It can be considered either to be a problem of initial conditions, of boundary values, or a combination of both. The conceptual differences and the scope of every approach are clearly discussed by Chang et al. (2000). The boundary value approach for forecasting by means of an atmospheric model and considering the sea-surface temperature (SST) as the single forcing is, theoretically, almost equivalent to suppose the coupling of an imperfect atmospheric model with a perfect oceanic model. In practice, the forecast of climate anomalies requires the forecast of the SST, either through the oceanic models run independently or interactively with the atmospheric model. The hindcast of climate anomalies using atmospheric models forced with observed SST data provides an important piece of information: The skill of the atmospheric model can be considered as the maximum skill attainable when coupled to any oceanic model for the forecast of climate anomalies. The inclusion of the initial conditions of the system and the boundary condi-

tions in the soil-atmosphere interface, controlled by factors as diverse and heterogeneous as the physical properties and state of the soil, type and physiological status of the vegetation, and terrain topography, adds new challenges to the problem (Anderson and Ploshay 2000).

Numerous atmospheric numerical experiments of the 'boundary values problem' type were reported in the Atmospheric Model Intercomparison Project (AMIP; Gates et al. 1999). These were carried on with different AGCM forced with the observed SST. The results of these experiments concur on the forced predictability strength in tropical oceanic areas. Climate statistics in certain extratropical areas still depend on the anomalies in the tropical SST, especially during ENSO episodes, when these anomalies acquire great intensity and extent. For instance, the research by Anderson et al. (1999) provides evidence of this dependence for the Pacific–North American (PNA) pattern region. The cause of the diminution of the forecast ability in middle and high latitudes is partially attributed to an intrinsic characteristic of the climate system: The increasing intensity of the noise generated by short time-scale random weather fluctuations relative to the intensity of the climate signal produced by slowly changing external forcing factors (Leith 1978).

From 20° to 40°S, the zonal averages of the meridional fluxes of momentum, heat and humidity due to transient eddies increase in magnitude and overlap the fluxes due to the stationary eddies and to the mean meridional circulation (Peixoto and Oort 1992). This behavior is particularly observed over the South American continent, where transient eddy activity can be a determinant factor of the local climate and of its interannual variability (Labraga et al. 2000). Thus, the evaluation of the skill to simulate climate anomalies should include not only mean fields but in addition those second-order moments that are more relevant to the description of the climate in these latitudes.

The objective of this work is to evaluate the capability to simulate climate anomalies, for atmospheric dynamic and thermodynamic variables, of seasonal (three-month) scale over the South American Continent and neighboring oceanic areas, using an ensemble of integrations of an AGCM forced with the observed SST. Recently, Marengo et al. (2003) have assessed the seasonal rainfall predictability over several regions of the world, including South America, using a similar procedure with an ensemble of nine integrations. The South American Continent, extending approximately between 15°N and 55°S, offers an interesting scenario for simulation skill assessment in tropical and extratropical regions. Besides, the ENSO signal, one of the most important sources of climate interannual variability, is clearly present throughout South America. It is possible to identify wide continental regions with significant anomalies of opposite sign in each one of the ENSO phases that are related to atypical large-scale circulation patterns (Grimm et al. 2000). This increases the interest in the predictability of rainfall distribution over South Amer-

ica, severely and unevenly affected over densely inhabited regions during these events.

Following section contains a summary of the main characteristics of the AGCM used in this research. Section 3 describes the characteristics of the numerical experiment and defines the statistical measures of skill and the reference data sources used in the simulation evaluation. Section 4 is dedicated to the presentation of results. This includes brief description of the model systematic errors, detailed account of the signal-to-noise ratio pattern in the study region and analysis of simulation skill variations with the ensemble size and within the period and area of study. The model performance during the ENSO phases is compared with that of the neutral periods. Besides, the ability to reproduce anomalies in variance and covariance fields that represent relevant extratropical climate processes is thoroughly examined. Obtained results are discussed and summarized in Sect. 5.

Model description

The model used in the numerical experiment is the AGCM CSIRO Mark 2, thoroughly described in McGregor et al. (1993) and Watterson et al. (1995). Following is a summary on its main characteristics. The model's equations are solved through spectral methods, and its code allows the use of different horizontal and vertical predetermined resolutions. The formulation of the atmospheric dynamics equations in its flux format insures the mass conservation. The model includes the treatment of the following physical processes: daily and annual radiation cycles, shallow and deep convection, atmospheric gravity wave drag, and parameterization of subgrid-scale turbulent vertical mixing. It makes use of a vectorized version of the radiation code developed at the Geophysical Fluid Dynamics Laboratory, with computation of long-wave radiation based on Schwarzkopf and Fels (1991) and short-wave radiation based on Lacis and Hansen (1974). A modified version of Arakawa's (1972) moist convective adjustment scheme assumes mass flux between the base and top layers of the convective column and generates vertical moisture and momentum redistribution. A Semi-Langrangian representation of the atmospheric water vapor transport has been incorporated (McGregor 1993). It has linked a soil model capable of forecasting the surface temperature and of diagnosing the moisture content. The modeling of the surface fluxes over land differentiates bare soil from soil covered by a vegetation canopy (Kowalczyk et al. 1994). The sea-ice model, also integrated to the atmospheric model, provides a dynamic and thermodynamic treatment of the main physical processes in this component of the climate system: vertical and lateral growth/ablation, growth due to snow deposit, convergence/divergence, and advection (O'Farrell 1998; Watterson et al. 1997).

Experimental design and evaluation method

The model was run with the horizontal resolution corresponding to a spectral rhomboidal truncation R21 (approximately $3.2°$ latitude $\times$ $5.6°$ longitude) and nine not uniformly spaced sigma levels that determine a vertical resolution which increases toward the surface. Even though the model has been prepared for running with higher resolution, computer-time demand resulting from the length and the number of projected simulations imposed a limitation to resolution. The numerical experiment is comprised by an ensemble of 20 simulations forced by the global daily SST observed between January 1986 and December 1998. The SST data, based on the weekly analysis of Reynolds and Smith (1994) linearly interpolated to daily values, were obtained from NOAA-CIRES Climate Diagnostic Center at http://www.cdc.noaa.gov/PublicData/. Every member of the ensemble is the output of a 13-year simulation started on 1 January 1986, using different model equilibrium conditions taken from different years of a previous long control run forced by the annual climate cycle of the SST. The memory of the atmospheric initial conditions almost vanishes approximately after a month of model integration. In this work, the attention is focused on the ability to reproduce seasonal-scale climate anomalies and the use of observed initial conditions is not considered relevant on a first stage. The first year of each simulation is considered as a period of adjustment of the atmosphere-soil-sea-ice system, and is not taken into account in the evaluation of the simulation capability.

Simulated temperature, geopotential height and wind components at several pressure levels were compared to data obtained from the NCAR/NCEP Reanalysis (Kalnay et al. 1996). Rainfall data from Reanalysis are a model product obtained from 6-h forecasts. For that reason, it was preferred to compare model rainfall with the Climate Prediction Center Merged Analysis of Precipitation data (Xie and Arkin 1997), based on gauge observations, satellite estimates and numerical model output. These data were obtained at the NOAA-CIRES Climate Diagnostic Center website. The assessment of simulated second-order moments, computed with 4-daily deviations from monthly mean values, was accomplished comparing with data also from the NCAR/NCEP Reanalysis.

The study region extends from $180°W$ to $10°W$ and from $15°N$ to $60°S$, and covers the whole South American Continent, the west of the Atlantic Ocean and a wide sector of Pacific Ocean that includes the ENSO epicenter.

The correlation coefficient ACC_t and the root-mean-square error RMS_t are the statistical measures of similarity among patterns used to evaluate model skill. A total of 143 3-month running mean values was considered in the assessment. All measures of skill are computed for the ensemble mean. The coefficients are defined as in Anderson et al. 1999:

$$ACC_t = \frac{\left[\sum_i \alpha_i (F_i - C_i)(O_i - C_i) \right]}{\left[\sum_i \alpha_i (F_i - C_i)^2 \sum_i \alpha_i (O_i - C_i)^2 \right]^{1/2}} \quad (1)$$

$$RMS_t = \left[\frac{\sum_i \alpha_i (F_i - O_i)^2}{\sum_i \alpha_i} \right]^{1/2} \quad (2)$$

where F_i are model values, O_i observed values, C_i climate-mean-observed values, α a coefficient depending on the latitude that weighs the area represented by the ith grid point. The summation extends over all grid points within the region of the study and the atmospheric level considered, and subindex t indicates the 3-month mean evaluated. The climate mean C is locally computed over the experimental period excluding the tth value, as required by the crossvalidation procedure.

Two other local statistical measures of similarity are defined to quantify variations of the simulation skill within the study region. These are the time correlation between anomalies ACC_i, and the root-mean-square error RMS_i at the ith grid point, defined as:

$$ACC_i = \frac{\sum_t (F_t - C_t)(O_t - C_t)}{\left[\sum_t (F_t - C_t)^2 \sum_t (O_t - C_t)^2 \right]^{1/2}} \quad (3)$$

$$RMS_i = \left[\frac{1}{N-1} \sum_t (F_t - O_t)^2 \right]^{1/2} \quad (4)$$

where variables F, O and C have the same meaning than in Eqs. 1 and 2, the calculation of C satisfies the previous crossvalidation procedure, t is a time index varying from 1 to $N = 12$ (number of years used in the assessment) for each 3-monthly mean from DJF to SON, and subindex i indicates the grid point considered. It is impractical to show maps for every 3-month mean, variable and type of statistic considered. Annual averages of 3-monthly skill coefficients are shown in the following figures that concisely illustrate many important features observed throughout the year while the most outstanding seasonal variations are pointed out in the text.

Gross systematic errors in simulated values F_i were corrected before the computation of ACC. The systematic error correction is simply the difference between model and observed climate means computed with the above-mentioned crossvalidation constraint. This correction is equivalent to use the model climate mean instead of the observed climate mean in $(F_i - C_i)$ in Eqs. 1 and 3.

In order to calculate the statistical measures, it was necessary to interpolate the reference data from their finest grid ($2.5°\times2.5°$) to the spaced grid of the model. Additionally, for comparisons at different atmospheric levels, it was necessary to interpolate model output from sigma levels to standard pressure levels.

Results

Model systematic errors can be statistically corrected using different approaches. However, it is worth to consider them carefully since space and time distributions of errors help to uncover model weaknesses or limitations and to explain statistical results about model performance. The distribution of the already mentioned signal-to-noise ratio is another factor inherent to the climate system, which modulates the simulation capability. Both factors are analyzed in the following two sections before examining results on statistical measures of performance for a selection of atmospheric variables.

Distribution of the model systematic error

Labraga and Frumento (2003), hereafter LF2003, carried out a 30-year climate experiment with the CSIRO Mark 2 atmospheric model coupled to a dynamic ocean model. The purpose of that experiment was to assess model skill in the simulation of the contemporary climate of South America. Conditions at the ocean–atmosphere interface were freely determined by surface-flux exchanges between both models (free simulation). For that reason, the simulated atmospheric variability does not represent the observed behavior in any particular period. In the current experiment, SST data observed between 1986 and 1998 are used as a boundary condition for the atmospheric model, and climate anomalies thus generated are compared with observed anomalies in the same period. In spite of conceptual differences between both experiments, simulated climates can be compared with observations and to each other to search for model systematic errors.

The same observed datasets reported in Sect. 3 were used to compute model systematic errors in both experiments, relative to 1969–1998 means in the first case and to 1986–1998 means in the second case. The error distributions within the region of the study exhibit very similar features, which are probably dependent on model characteristics such as physical parameterizations or space resolution. Only those aspects that are relevant to the purpose of the present work will be summarized next (see LF2003 for details).
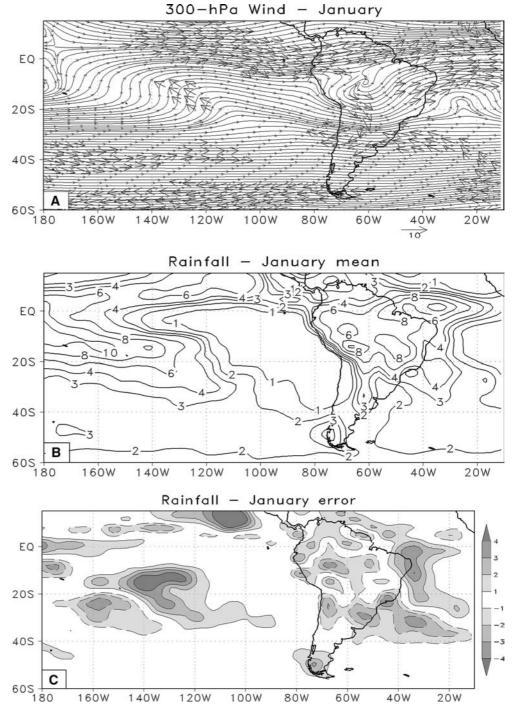
The likeness between the systematic errors in the free run of the coupled model and in the forced run of the atmospheric model is reasonable, since in the coupled run systematic corrections were applied in the surface fluxes computed at the ocean–atmosphere interface and in the ocean temperature and salinity to reduce to the maximum the climate drift (Gordon and O'Farrell 1997). This, however, are weaker constrains than the use of observed SST as boundary condition.

An important climate aspect to consider is the simulation of the monsoon circulation during the Southern Hemisphere summer months. Zhou and Lau (1998) proposed a phase partition of the 1989–1990 South

American monsoon and considered 30 Dec 1989 to 7 Feb 1990 as the mature phase. The Bolivian Anticyclone and the Nordeste trough are two features distinguishable in the January mean circulation at 300-hPa level in Fig. 1a. However, it should be noted that the center of the anticyclone is displaced about 5° to the North in comparison to the NCAR/NCEP Reanalysis, a model bias which is likely to produce additional local climate departures. This is the cause of the excessive westerly wind to the south of the Bolivian Anticyclone center. The intensity of the subtropical jet stream over the southeast of the continent and over the west of the South-Atlantic Ocean is underestimated in this month and also in the winter-time circulation (not shown in the figure). At higher latitudes, the modeled intensity of the subpolar jet stream is also lower than in the reanalysis.

Consistently, with the development of the monsoon circulation, the model acceptably reproduces rainfall-rate distribution, although some considerations should be made in this regard. Figure 1 shows the January mean field (Fig. 1b) and systematic error (Fig. 1c) in one of the rainiest months in the continental area. Convective activity seems to be underestimated over the Amazon River basin, where simulated rainfall rate is 20–30% lower than the observed and is similarly overestimated over Northeast Brazil. In the Southeastern sector of the continent comprising entire Uruguay, northeast of Argentina and the south end of Brazil, the model also displays a significant negative rainfall bias. This deficit is observed throughout the year and could be linked to a different cause than the negative bias over the Amazon basin, which is likely linked to the model convective scheme, and will be examined later.

Over the oceans, the most important features are the rainfall maximum associated with surface convergence like the Intertropical Convergence Zone (ITCZ), the South Pacific Convergence Zone (SPCZ) and the South Atlantic Convergence Zone (SACZ). The model reproduces reasonably well the rainfall magnitudes, but even small errors in the location of these narrow bands of intense convection produces large systematic errors. The simulation of a less-pronounced southeastward tilt or a northward shift in the SPCZ and in the SACZ compared to the observations produce parallel bands of opposite sign errors over the oceans (Fig. 1c). The SPCZ shifts just in the direction of the observed precipitation gradient causing larger positive errors on the equatorial side. Similarly, positive errors in the eastern equatorial Pacific are caused by an excessively northward location of the ITCZ in this season. In the austral ocean, the model slightly overestimates the rainfall rate in winter (not shown in figures), but the veracity of the data on this region is uncertain.

Model rainfall departures from observed values depicted for continental regions (Amazon basin, northeast Brazil, and Southeast of the continent), the convergence zones (SPCZ, ITCZ and SACZ) and the southern oceans are very similar to those found by Cavalcanti et al. (2001) using the CPTEC-COLA AGCM, errors of

Fig. 1 a Simulated 300-hPa mean flow (streamlines) and model systematic error (vectors) for January. *Error scale* is indicated on the right lower corner in m s^{-1}. **b** Simulated January mean rainfall rate in mm day^{-1} (*contour lines*). **c** Systematic error for January rainfall rate indicated with *gray shading* and full (*dotted*) contour lines for positive (negative) errors. Errors shown for the wind magnitude and the rainfall rate are significant at 5% level, according to the Student *t*-test for differences of sample means applied locally

which they partly attribute to the model convective scheme.

Systematic errors were also computed for three second-order moments: mean sea level (MSL) pressure variance $<p'^2>$, 850-hPa level covariance between meridional wind component and temperature $<v'T'>_{850}$ and 850-hPa level covariance between meridional wind component and specific humidity $<v'q'>_{850}$. These second-order moments and levels were chosen because they are good indicators of mean cyclonic activity and meridional eddy transport of heat and humidity. Computations were made for DJF, MAM, JJA and SON using four-daily deviations relative to the monthly mean. For brevity, Fig. 2 shows only simulated annual mean fields and model systematic errors.

The model adequately reproduces the known MSL pressure variability increase with latitude up to a maximum located between 55° and 60°S, almost below the subpolar jet stream maximum (Hurrel et al. 1998).

Fig. 2 a Variance of MSL pressure data $<p'^2>$ (in hPa^2). **b** Covariance between meridional wind component and temperature $<v'T'>_{850}$ at 850-hPa level (in $Km\ s^{-1}$). **c** Covariance between meridional wind component and specific humidity $<v'q'>_{850}$ at 850-hPa level (in $g\ Kg^{-1}\ m\ s^{-1}$). Statistics are computed with 4-daily departures relative to the monthly mean. *Thick contour lines* indicate simulated climate mean fields. The *gray shading* and full (*dotted*) contour lines indicate positive (negative) model systematic errors. Errors shown in the figure are significant at 5% level

However, the intensity of this maximum is slightly lower than the observed. The axis of maximum $<v'T'>$ and $<v'q'>$ covariances in the Pacific Ocean (Fig 2) are less southeasterly tilted than in observations, producing the negative bias in the region. The southward eddy-flux in Fig. 2 is negative, thus negative errors mean underestimated southward flux.

The signal-to-noise ratio pattern

The sensitivity of the extratropical response of an atmospheric model to SST forcing depends largely on the relation between the amplitude of the boundary-forced climate signal and the amplitude of the internal noise resulting from the uncertainty in the initial

conditions. The climate signal amplitude can be estimated by the interannual variance of the ensemble mean with respect to the climate mean, which is defined as follows:

$$S_s^2 = \frac{1}{N-1} \sum_{i=1}^{N} (\overline{x_i} - \langle \overline{x} \rangle)^2 \qquad (5)$$

In this and the following equations, x represent DJF, MAM, JJA or SON mean values, the upper bar indicates average over the m members of the ensemble and the brackets time average over the N-year experimental period.

The internal noise amplitude is estimated by the mean intra-ensemble variance, defined as:

$$S_n^2 = \frac{1}{N(m-1)} \sum_{i=1}^{N} \sum_{k=1}^{m} (x_{ik} - \overline{x_i})^2 \qquad (6)$$

where m is the size of the ensemble. The signal-to-noise ratio is defined as the following:

$$\text{SNR} = \frac{S_s^2}{S_n^2} \qquad (7)$$

SNR is not a measure of model skill; it is commonly considered as a measure of potential predictability: it is feasible to find good simulation skill in those regions where climate signal amplitude is significantly superior to noise amplitude. Assuming that we are dealing with normally distributed random variables, then mSNR is also a random variable with an F-distribution and $(n-1, n(m-1)$ degrees of freedom. Therefore, in this case $(N=12, m=20)$, the 5% of the signal statistical significance is reached for $F_{11, 228} (0.05) = 1.8$, equivalent to SNR = 0.09. In the following figures, SNR values greater or equal than 0.25 are shaded, to point out regions where acceptable skill is expected.

It is interesting to compare SNR obtained for different atmospheric variables that characterize the thermodynamic and dynamic state of the climate, and for different levels in the troposphere. Computations were made according to Eqs. 5, 6, 7 definitions and for JFM, AMJ, JAS and OND separately. However, for sake of the briefness, Fig. 3 shows annual mean SNR fields, and the most important seasonal features are commented in the text.

In the South Pacific Ocean between 170°W and 120°W and between the tropical region and the Antarctic coast, the SNR for 850-hPa temperature, 500-hPa geopotential height and 300-hPa zonal wind exhibits a basic pattern composed by three relative maximums. One of the maximums is located straddling the equatorial line. The other two are located at about 30° and 60°S for 850 hPa temperature and 500-hPa geopotential height, and at about 20° and 50°S for 300-hPa zonal wind component. In the equatorial Atlantic Ocean, there is an additional relative maximum near the continent, which in MAM expands over the Amazon River basin.

Rainfall rate shares some tropical characteristics with previous mean variables, such as the SNR absolute maximum in the equatorial Pacific Ocean between 120° and 170°W and a relative maximum over the equatorial Atlantic Ocean near the continent (Fig. 3d). In subtropical to mid latitudes of the Pacific Ocean and in the southwest Atlantic Ocean next to the Rio de la Plata mouth, SNR patterns for rainfall rate and for $<p'^2>$, $<v'T'>_{850}$ and $<v'q'>_{850}$ second-order moments participate in some common features (Fig. 4a, b, c). A belt of relatively high SNR extends in northwest–southeast direction almost parallel to the SPCZ. The axis of maximum SNR lies to the south of the rainfall maximum for $<v'T'>_{850}$, to the north of it for $<p'^2>$ and almost on top of it for $<v'q'>_{850}$. Relatively high signal amplitude is continuously found further east, between the Pacific Ocean Anticyclone and the westerly wind domain, the southern part of South America and the western Atlantic sector next to the Rio de la Plata mouth. Over the continent, SNR is above 0.2 in mid latitudes up to about 50°S, with greater meridional extension in JJA than in DJF, and relatively lower values to the east of the Central Andes.
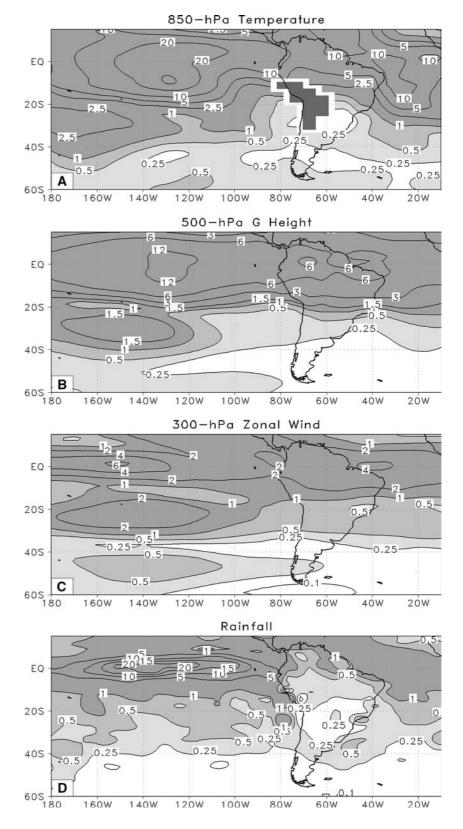
Some comments on the internal noise are appropriate for a better understanding of the SNR distributions illustrated in Fig. 3. For most variables, the noise amplitude S_n^2 has a rather simple distribution, which is exemplified in Fig. 5 for 500-hPa geopotential height, averaged over the year. S_n^2 increases with latitude up to a maximum located somewhere between 60°S and the Antarctic coast. The seasonal variation (not shown in the figure) is characterized by increase and northward shift of the highest noise levels. This pattern corresponds to the meridional and seasonal distributions of synoptic-scale disturbances. By definition (Eq. 6), S_n^2 is the variance of the ensemble components with regard to the ensemble mean or intraensemble variance, the source of which is the uncertainty in the initial conditions. This statistic can be considered as a measure of dispersion of the ensemble members.

The signal amplitude S_S^2 (not shown separately in figures) has three maximums distributed from equator to pole over the Pacific Ocean and one maximum over the equatorial Atlantic Ocean near the continent. The extratropical signal over the Pacific sector is stronger in JJA than in DJF. This distribution of signal amplitude, modulated by the noise distribution, produces the SNR patterns depicted in Fig. 3.

Simulation skill variation with the ensemble size

To assess the change of simulation skill with the ensemble size, ACC_t was computed as a function of the ensemble size or number of simulations m for 500-hPa geopotential height. Computations were made for the region between 180° and 10°W and three latitude belts: the total study area 60°S to 15°N, the intertropical re-

Fig. 3 Average of DJF, MAM, JJA and SON signal-to-noise ratio for **a** 850-hPa temperature, **b** 500-hPa geopotential height, **c** 300-hPa zonal wind and **d** rainfall rate. The *gray scale shading* indicates SNR greater than 0.25, 0.5 and 1. The *shaded box* over the continent in the *upper panel* indicates the intersection between model topography and the 850-hPa level
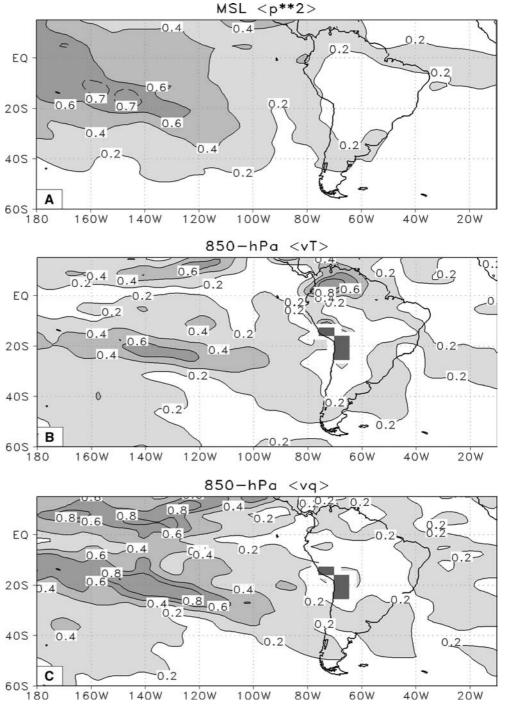

gion 23°S to 15°N and the extratropical region 60°S to 23°S, and results are shown in Fig. 6.

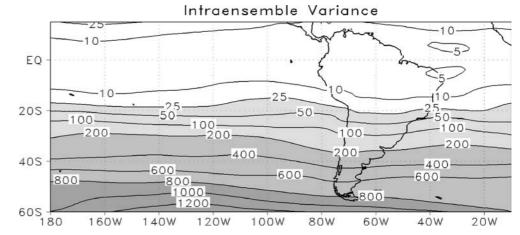ACC$_t$ is a measure of correlation between simulated and observed patterns for a given quarterly mean field

(DJF, MAM, JJA or SON) and a given year t. Each point on the curve represents the average of all quarterly values of ACC$_t$ over the complete experimental period. When m is small, the average value of the coefficient

Fig. 4 Average of DJF, MAM, JJA and SON signal-to-noise ratio for **a** $<p'^2>$, **b** $<v'T'>_{850}$ and **c** $<v'q'>_{850}$. The *gray scale* shadings indicate SNR greater than 0.25, 0.5 and 1

obtained in this way is rather sensitive to the model performance in each particular simulation and it can vary extensively depending on the m runs selected among the 20 available in the ensemble. In order to increase result stability, each point on the curve was recalculated as the average of ACC_t over a maximum of 50 'synthetic' ensembles, each one of which has m components . Each element in the new ensembles is a 12-year time-series generated through random combinations without repetition of monthly means picked out sequentially from the pool of 20 simulations of the 1986–1998 period.

Over the whole region, simulation skill increases rapidly while the ensemble size increases up to about 10 and rather slowly thereafter, however, without reaching saturation. Using the "perfect model" approach and 500-hPa geopotential height data, Déqué (1997) finds a similar ACC behavior in the size range from 1 to 9, and he estimates that 90 percent of the asymptotic value could be reached with 20 components. Results obtained in this work indicate that this could be true in the intertropical region, but in the extratropical region, the simulation ability seems to be increasing even for ensemble size 20, although variations occur very slowly.

The skill improvement achievable by increasing the size of the ensemble beyond 20 runs implies a considerable increment in computer-time demand.

Regional mean skill

The performance of the model for each variable and within the study region as a whole can be measured averaging all ACC_t and RMS_t quarterly values over the 12-year simulation. In order to allow the comparisons between different variables and atmospheric levels, the RMS was normalized by the observed local standard deviation (NRMS). Results of these statistical measures are shown in Table 1.

The simulation skill for a given variable improves with the distance from the surface and this is exemplified in Table 1 for 500-hPa geopotential height. Similarly, the simulation ability of surface temperature anomalies is relatively lower than for 850-hPa temperature. At the 850-hPa level the simulation skill for temperature is
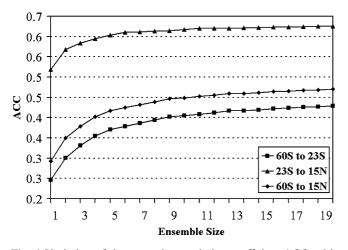
better than for geopotential height. This is reasonable since the atmospheric model is forced by the SST. The 300-hPa zonal wind shows correlation and error values that corroborate a general better performance in the high troposphere. It is encouraging to find out capability to reproduce rainfall-rate anomalies comparable to other variables, considering the severe difficulties involved in the parameterization of convection and other rainfall-related processes and their characteristic scales being much lower than the model spatial resolution.
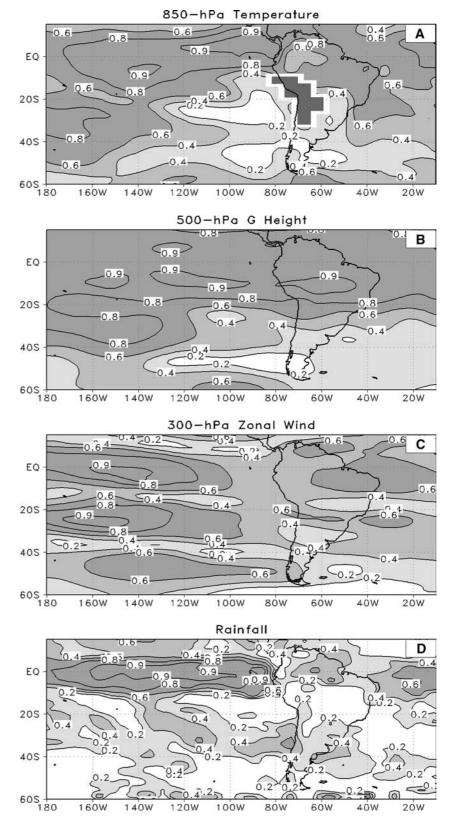
Local simulation skill

Figure 7 shows the ACC_i patterns for the 850-hPa temperature, 500-hPa geopotential height, 300-hPa zonal wind and rainfall rate. ACC_i was computed separately for DJF, MAM, JJA and SON in order to consider seasonal variations, although for brevity the figure shows the characteristics of the annual mean fields.

The regions with better simulation performance are approximately in correspondence with those with higher SNR as expected (compare with Fig. 3). For instance, the higher modeling skill in the intertropical zone between 20°S and 15°N is noticeable in general, with an absolute maximum in the equatorial Pacific Ocean, a relative maximum in the equatorial Atlantic Ocean near the continent, and a marked decline in performance quality with increasing latitude. Secondary maximums

Fig. 6 Variation of the anomaly correlation coefficient ACC_t with the ensemble size (see details of computation procedure in the text), for the 500-hPa geopotential height in the region from 180° to 10°W and for three latitude belts: 60°S to 15°N, 60°S to 23°S and 23°S to 15°N

Table 1 Regional mean skill measured by the average of ACC_t and $NRMS_t$ (see text for definitions) over 143 3-month values computed between 1987 and 1998 for different variables and levels

Variable	ACC	NRMS
850-hPa temperature	0.54	0.84
850-hPa G. height	0.37	0.93
500-hPa G. height	0.47	0.87
300-hPa G. height	0.51	0.85
Rainfall rate	0.46	0.92
300-hPa zonal wind	0.51	0.86

Fig. 7 Anomaly correlation coefficients ACC$_i$ for: **a** 850-hPa temperature, **b** 500-hPa geopotential height, **c** 300-hPa zonal wind and **d** rainfall rate. The coefficients were computed with all 3-month running mean values comprised in the experimental period (see definition in the text). The *gray scale shading* indicates ACC$_i$ greater than 0.2, 0.4 and 0.6

in mid and high latitudes of the South Pacific Ocean in the first three variables are also noticeable, in correspondence with the SNR pattern.

The highest simulation ability for rainfall rate (Fig. 7d) occurs over the eastern equatorial Pacific Ocean, where the close correspondence between rainfall and SST anomalies is well known .Within the equatorial zone, the correlation is relatively high also over the continent and the West Atlantic Ocean. The model performance over the SACZ during its most active

period in DJF (not shown in the figure) was not found to be satisfactory.

Rainfall also exhibits a narrow belt of relatively high ACC crossing the study region, with a maximum skill axis between 180°W, 15°S and 40°W, 40°S. This band traverses the continent and includes the regions with ACC greater than 0.4 near the Pacific and Atlantic coasts. This feature is consistent with the SNR distribution in the same region (Fig. 3d).

To take into account the sensitivity of the previous results to the choice of the measure of skill, the $NRMS_i$ field of each variable was also computed. Both coefficients are inversely related: when ACC approaches its upper limit $+1$, NRMS becomes much smaller than 1, and when ACC decreases to zero or takes negative values NRMS becomes much greater than 1. The analysis revealed that both of the statistical measures exhibit very similar patterns within the region of study and for that reason results will not be presented here in detail. Regional mean values can be compared in Table 1. However, a comment about $NRMS_i$ fields is appropriate. This measure of skill seems to be more effective than ACC_i to reveal small-scale features. This is illustrated in Fig. 8 with the NRMS field for 500-hPa geopotential height. Between 20°S and 15°N, it takes values smaller than 1 in correspondence to ACC values greater than 0.8 in Fig. 7. However, within this latitude belt the lowest errors occur symmetrically in 10°S and 10°N and a relative maximum is noticed over equator in the Pacific Ocean; details are not easily discernible in the corresponding ACC field in Fig. 7. The NRMS for rainfall rate (Fig. 8b) lets us discern more clearly than does ACC (Fig. 7d) the relatively high skill belt stretching from low to mid latitudes over the Pacific Ocean and crossing the southern part of the continent toward the Atlantic (light gray-shaded region with NRMS < 1).

Modeling skill for second-order moments

In mid latitudes in general and in the stormtrack zones in particular, synoptic perturbations account for the most of the meridional transport of momentum, heat and humidity, dynamics processes with a dominant influence on the extratropical climate. A useful piece of information is, then, the modeling ability of seasonal anomalies in the intensity of the cyclone activity or in the location of the stormtracks. Efficient indicators for these features may be obtained from the daily MSL pressure variance about the monthly mean $<p'^2>$. Anomalies in the meridional transports of heat and humidity due to synoptic disturbances are traceable in $<v'T'>_{850}$ and $<v'q'>_{850}$ covariance fields respectively. A representative level for assessing model skill in the simulation of anomalies in these transports may be, for instance, 850-hPa. Figure 9 shows the ACC fields obtained for these second-order moments, computed with the same procedure applied for three-monthly mean variables.

Over the continent and adjacent oceans, $<p'^2>$ and $<v'q'>_{850}$ anomalies are better simulated between about 20°S and 50°S than elsewhere. A similar relative

Fig. 8 Root-mean-square error coefficients normalized by the observed standard deviation $NRMS_t$ for: **a** 500-hPa geopotential height, and **b** rainfall rate. The coefficients were computed with all 3-month running mean values comprised in the experimental period (see definition in the text). The *gray scale shading* indicates $NRMS_t$ smaller than 1, 0.8, 0.6 and 0.4
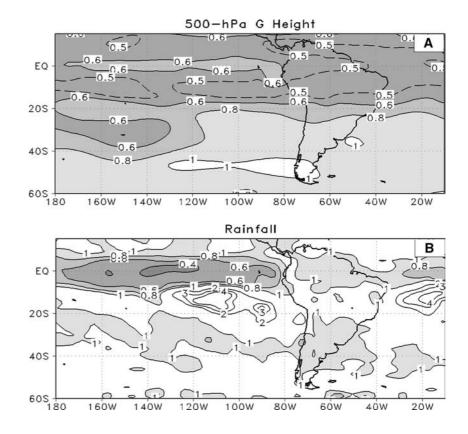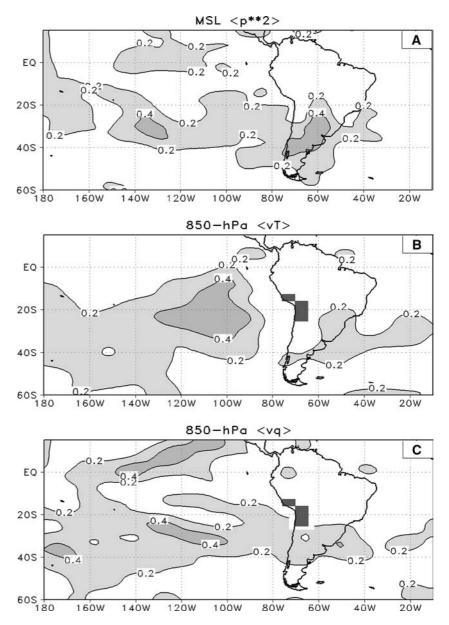
maximum was noted in the extratropical simulation of rainfall. This performance is different from that of other mean variables, which in general exhibit the best skill over the continent at low latitudes. Correspondence between SNR and ACC patterns in the Pacific Ocean sector is evident for $<v'q'>_{850}$ and $<p'^2>$ and less obvious for $<v'T'>_{850}$, regarding the existence of an axis of relatively high skill in the Pacific Ocean which extends in northwest–southeast direction between about 180° 15°S and 40°W 40°S.

Time variation of the performance level

The similarity between simulated and observed anomaly patterns varies widely during the experimental period. Time series of 3-monthly ACC$_t$ values are shown in Fig. 10 for 850-hPa temperature, 500-hPa geopotential height, 300-hPa zonal wind, and rainfall rate. The series fluctuate mostly between −0.2 and 0.8, with occasional larger departures. However, a quite defined variation pattern can be noticed, characterized by periods of relatively high correlation, i.e., higher than 0.5, separated by periods of low and fluctuating correlation. For example, during years 1988–1989, 1991–1992 and 1997–1998, there are periods of continuously high performance, while during years 1990, 1993 and 1995 ACC$_t$ takes very low values. Anderson et al. (1999) found similar variability in the skill coefficient for 700-hPa geopotential height in the approximately symmetric NH region known as the PNA region. In the ACC$_t$ time series for precipitation, this behavior is less obvious. As it will be seen in next section, the best performance generally occurs during the ENSO events.
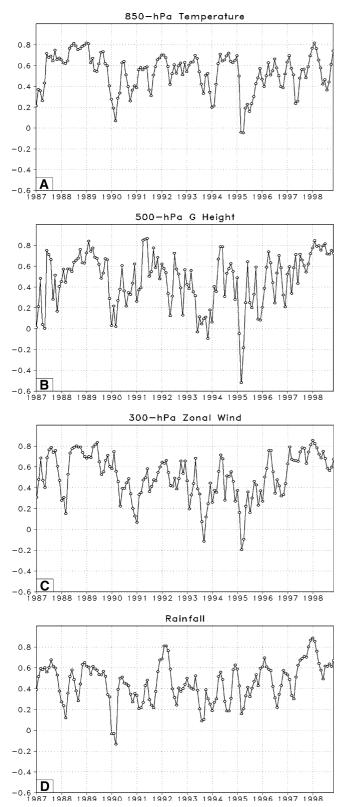
Fig. 10 Temporal variation of the anomaly correlation coefficient ACC_t (refer to definition in the text) for: **a** 850-hPa temperature, **b** 500-hPa geopotential height, **c** 300-hPa zonal wind and **d** rainfall rate, for every three-monthly running mean between 1987 and 1998
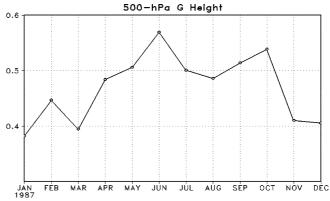

Fig. 11 Mean annual variation of the anomaly correlation coefficient for the 500-hPa geopotential height
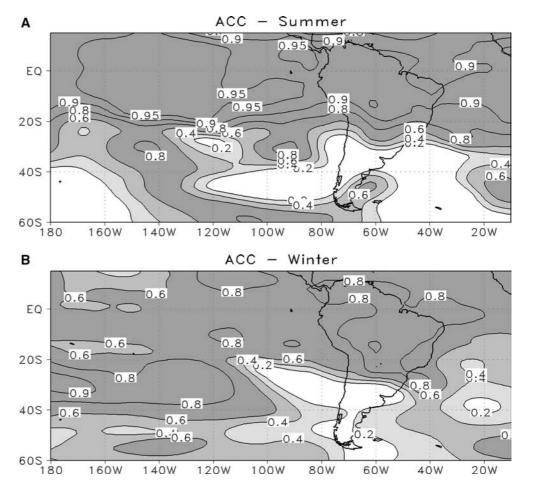
The simulation skill shows a typical annual cycle in this model, obtained averaging ACC over 12 simulated years and exemplified in Fig. 11 for 500-hPa geopotential height. The amplitude of the annual cycle is very small compared to interannual fluctuations. The Geopotential height of different pressure levels and 300-hPa zonal wind present similar annual cycles. The best performance occurs from May to October, with maximum ACC in June. Anderson et al. (1999) also found higher ACC levels for 700-hPa geopotential height in the PNA region during the NH winter and beginning of spring. The annual cycles for 850-hPa temperature and rainfall rate (not shown in figures) have amplitudes of about 0.1. For the 850-hPa temperature, the skill is slightly higher in the SH summer and for the rainfall rate the best performance takes place during autumn and summer.

The seasonal change in the local level of performance, as measured by ACC_i, is illustrated in Fig. 12 for 500-hPa geopotential height during summer and winter. Performance level is greater in the SH summer than in winter in the intertropical zone, especially in the central Pacific Ocean where ACC_i changes from 0.6 in JJA to 0.95 in DJF. Performance level is lower in summer than in winter in the latitude belt between 20° and 50°S, except for the extreme south of the continent.

Simulation skill during ENSO events

From early 1987 to late 1998, five El Niño and three La Niña well-defined events occurred. The starting and ending dates of each event, determined according to the Trenberth (1997) criterion based on the magnitude of the SST anomalies in the El Niño-3.4 region, are shown in Table 2.

The likeness between simulated and observed patterns in each ENSO phase and during the non-ENSO periods can be quantified through regional mean values of ACC, shown in Table 3. It should be recalled that this

Fig. 12 Anomaly correlation coefficient ACC$_i$ for 500-hPa geopotential height, in SH summer (*upper panel*) and winter (*lower panel*)

measure of skill was obtained from all 3-month mean fields comprised in each occurrence and type of event. Thus, the highly seasonal dependent characteristics of warm and cold ENSO phases are taken into account in this assessment.

Simulation skill is higher during ENSO than during non-ENSO periods in all the variables considered. The superior performance is consistent with higher *SNR* levels in most variables, as shown in the same table. From Table 3 it is inferred that the anomalies during La Niña events are reproduced more efficiently than during El Niño, although the difference in sample size may be too large to affirm this categorically.

Some questions arise from previous results as to how the general skill pattern changes and where simulation capability improves from neutral to ENSO periods. These questions can be figured out comparing ACC$_i$ fields for ENSO and No-ENSO events. Two variables were chosen for this purpose, 500-hPa geopotential height and rainfall rate, and results are shown in Fig. 13. The most dramatic changes in the simulation capacity take place over the Pacific Ocean. There, the amplitude of the relative maximums of ACC$_i$ located between the equatorial and Antarctic coastal zones along the climate

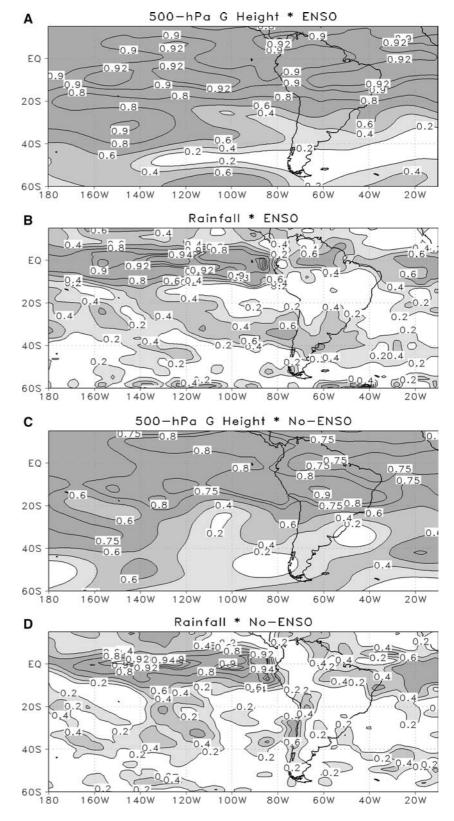**Table 2** Starting and ending month of El Niño and La Niña events between 1987 and 1998, according to the Trenberth (1997) criterion based on the magnitude of the SST anomalies in the Niño-3.4 region

El Niño	La Niña
Jan/1987–Feb/1988	Mar/1988–Jun/1989
Mar/1991–Jul/1992	Sep/1995–Mar/1996
Feb/1993–Sep/1993	Aug/1998–Nov/1998
Jun/1994–Mar/1995	
Apr/1997–May/1998	

Table 3 Anomaly correlation coefficient ACC, and signal-to-noise ratio SNR, averaged over the study region, for 3-monthly forecasts during the warm and cold phases of the ENSO events, separately and as a whole, and in non-ENSO periods between 1987 and 1998. The number of 3-monthly means in each case is indicated in parenthesis

	El Niño (63)		La Niña (27)		ENSO (90)		No-ENSO (53)	
	ACC	SNR	ACC	SNR	ACC	SNR	ACC	SNR
850-hPa temperature	0.57	7.6	0.62	21.1	0.58	8.1	0.47	2.9
500-hPa G. height	0.48	5.5	0.60	9.5	0.51	5.0	0.40	1.8
Rainfall rate	0.50	1.9	0.56	8.7	0.52	1.8	0.37	1.8
300-hPa zonal wind	0.55	1.8	0.64	4.8	0.57	2.0	0.44	0.9

Fig. 13 Anomaly correlation coefficients ACC$_i$ for 500-hPa geopotential height and rainfall rate, separately computed with all 3-month running mean values belonging to ENSO and No-ENSO periods defined in Table 2. The *gray scale shading* indicates ACC$_i$ greater than 0.2, 0.4 and 0.6

signal propagation pathway are greater in ENSO cases than in neutral cases. This is illustrated in Fig. 13 for 500-hPa geopotential height. In particular, the out-standing geopotential height anomaly which develops over the Bellingshausen Sea and southeastern Pacific Ocean (Kiladis and Mo 1998) seems to be correctly simulated. Over the continent, simulation ability in ENSO cases mainly grows over the Amazon River basin

region and the Southeastern sector of the continent where the Rio de la Plata basin is located. Similar behaviors were found in ACC_i fields for 850-hPa temperature and 300-hPa zonal wind component, which have not been shown in the figure. It is interesting to point out that a substantial part of the increment in the regional mean value of ACC for rainfall rate indicated in Table 3 takes place in the continental area over the just mentioned two main river basins, as can be noticed in Fig. 13.

Summary and discussion

An ensemble of 20 simulations has been made with the CSIRO Mark 2 atmospheric model, forced by the SST observed during the 1986–1998 period. The purpose of the experiment was to assess model ability to simulate seasonal scale climate anomalies over the South American continent and bordering oceans. The model skill is statistically measured through the anomaly correlation coefficient ACC and the RMS error normalized by the observed standard deviation. The signal-to-noise ratio distribution is compared with the simulation capability within a southern hemisphere area strongly influenced by the ENSO events. In these regards, this area has been less investigated than that of its counterpart, the PNA region, in the northern hemisphere.

The model bias in the simulation of the climate mean fields was analyzed prior to examine its capability to reproduce the seasonal climate anomalies. The systematic error patterns found in this ensemble of simulations with prescribed SST, are very similar to those found by LF2003 in a 30-year simulation with temperature at the sea–atmosphere interface determined by free interactions between atmospheric and oceanic models. A thorough error analysis carried out in the reference work agrees with the results obtained in this experiment regarding model capability to reproduce the outstanding features of the South American climate, a necessary though not sufficient condition for good climate anomaly simulations. The essential aspects of the monsoon circulation that regulates the annual cycle of the tropical and subtropical rainfall are acceptably modeled. However, in the previous work, it was found that the low horizontal resolution used in the model run (the same used in this work) produces a smoothed representation of the prominent Central Andes topography. This, in turn, causes an eastward displacement of the surface temperature maximum and a westward shift of the MSL pressure minimum located in the subtropical part of the continent in summer. Consequently, the intensity of the Atlantic Ocean anticyclone circulation over the continent decreases together with the southward advection of humidity and rainfall rate to the east of the Central Andes (Fig. 1). Further effects are weakening of the mean meridional temperature gradient and baroclinicity of the circulation, which could cause a reduction of the modeled meridional eddy-fluxes of heat and humidity over the southeast sector of the continent (Fig. 2).

Negative bias in high-latitude $<p'^2>$ maximum (Fig. 2) is consistent with a less intense westerly wind component simulated in the high troposphere (Fig. 1) and the consequent reduction of mean flow baroclinicity. Similarly, the weakness of the westerly wind modeled in the subtropical jet stream over the Atlantic Ocean adjacent to the continent between 30° and 40°S is coherent with the negative bias in the pressure variability.

Underestimation of summer latent heating over the Amazon basin, as suggested by negative rainfall rate bias in Fig. 1, and an indirect effect of reduced Andes elevation in model's topography upon rainfall distribution over the continent, can combine to produce the northward shift of the Bolivian High center in January noted in the same figure (Lenters and Cook 1997; Labraga and Frumento 2003).

The signal-to-noise ratio is an important intrinsic characteristic of the modeled climate system and is an useful indicator of regions where it is feasible to obtain acceptable skill in climate anomaly simulations. The SNR pattern for 300-hPa zonal wind component, for instance, clearly resembles a wave train propagating southward from the equator. The SNR distribution for 500-hPa geopotential height is very similar to that obtained by Chang et al. (2000). They point out that high SNR in mid to high latitudes occur mainly within the ENSO influence zone, with a wave-like structure emanating from the tropical Pacific zone into both hemispheres. The deep southward propagation of the climate signal may contribute to the surprisingly high SNR values in the SH, compared to the NH, as noticed by Chang et al. (2000).

It was found that rainfall rate SNR (Fig. 3d) shares distribution characteristic of other mean variables in the equatorial region, and of $<p'^2>$, and $<v'T'>_{850}$ and $<v'q'>_{850}$ second-order moments in the extratropical region (Fig. 4). Of particular interest are the southeastward propagation of signal along the SPCZ and, further east, the relatively high SNR over the continent between central Chile and Rio de la Plata mouth. The potential predictability gap to the east of the Central Andes could be linked to a local unrealistic simulation of airflow–topography interactions due to the low model resolution used in this experiment.

Regional mean values of ACC and NRMS obtained in this study (Table 1) are similar to those reported by Anderson et al. (1999) for a comparable NH region such as the PNA. It was found, in general, better performance at mid and high levels than at low levels of the troposphere. The spatial distributions of these measures of skill (Figs. 7, 8) confirm robustness of SST forced simulation of climate anomalies over tropical ocean areas and fast deterioration of simulation ability toward mid and high latitudes. Signal propagation toward extratropical region makes possible good simulation skill in extratropical zones over the Pacific Ocean, which con-

form the wave-train pattern noted in SNR. Over the continental area located to the southeast of the Central Andes, a zone was found to be characterized by low simulation capability for mean variables at low levels. This is consistent with the above-mentioned SNR gap found in the same area.

This research indicates that there is some simulation capability for anomalies in rainfall rate and $<p'^2>$, and $<v'q'>_{850}$ second-order moments over subtropical to mid latitudes of the Pacific Ocean and the southern part of the continent, in correspondence with relative SNR maximum. In order to understand this behavior, some regional circulation features should be taken into account. Intraseasonal and interannual deviations in the subtropical jet stream location and intensity over South America are linked to other important climate anomalies. The interaction of transient disturbances embedded in the westerly flow with the Andes Cordillera (Gan and Rao 1994) and land–sea thermal contrast in the Atlantic border of the continent generate a zone of baroclinic instability and remarkable cyclogenesis in the southeast of the continent and in the adjacent Atlantic sector (Berbery and Vera 1996). Then, anomalies in the cyclonic activity in this region can be linked to anomalies in the upper-level mean circulation. Simulation of low-level mean field anomalies cannot be efficiently accomplished, probably due to the low model resolution, as suggested above. However, performance improves appreciably in the upper troposphere, and ACC greater than 0.4 were obtained for 300-hPa zonal wind component between 20° and 40°S (Fig. 7c) where the subtropical jet stream axis can be found during part of the year over South America and the west of the Atlantic Ocean. Consistently, in these latitudes relatively high SNR and ACC values were obtained for second-order moments indicative of cyclonic activity and meridional eddy-transport of humidity (Figs. 4, 9), thus explaining the relatively high capacity to replicate rainfall anomalies over the continent between subtropical and mid latitudes. These results imply that part of the climate signal propagates through eddy-flux field anomalies, which thus becomes an important feature of climate prediction in extratropical regions.

Simulation efficiency presents wide variations during the 12-year simulation (Fig. 10). Simulation skill is greater during warm and cold phases of ENSO events than in neutral periods (Table 3), a behavior that resembles the one found by Shukla et al. (2000) for the 500-hPa geopotential height in the December–February quarter in the PNA region. The better performance in most of the variables is in correspondence with higher regional mean values of SNR. The ability to reproduce rainfall anomalies over the continent is relatively high in two regions: One extends from central Chile to the mouth of Rio de la Plata and approximately from 30°S to 40°S, and the other covers the northeastern part of the continent. Both regions are characterized by having almost coherent ENSO-related precipitation signal (re-gions 1 and 5 in Grimm et al. 2000, regions NSA and SSA in Ropelewski and Halpert 1987).

This work provides information about the real chances and limitations in the simulation of seasonal climate anomaly in the South American region, based on the CSIRO Mark 2 model results. The use of higher model resolution, in the horizontal as well as in the vertical, is an aspect currently under consideration that may lead to significant improvements, particularly over the low skill zone noticed over the Southeast of the continent. Useful rainfall anomaly simulations are feasible during El Niño/La Niña events over wide tropical and extratropical sectors of the continent. The obtained results are encouraging and justify tackling the most complex problem of climate forecast by means of coupled atmosphere–ocean GCMs.

References

Anderson JL, Ploshay JJ (2000) Impact of initial conditions on seasonal simulations with an atmospheric general circulation model. Q J R Meteorol Soc 126:2241–2264

Anderson J, Van den Dool H, Barnston A, Chen W, Stern W, Ploshay J (1999) Present-day capabilities of numerical and statistical models for atmospheric extratropical seasonal simulation and prediction. Bull Amer Meteor Soc 80(7):1349–1361

Arakawa A (1972) Design of UCLA general circulation model. Numerical simulation of weather and climate, technical report No. 7. Department of Meteorology, University of California, Los Angeles

Berbery EH, Vera CS (1996) Characteristics of the Southern Hemisphere winter storm track with filtered and unfiltered data. J Atmos Sci 53:468–481

Cavalcanti IFA, Marengo JA, Satyamurty P, Nobre CA, Trosnikov I, Bonatti JP, Manzi AO, Tarasova T, Pezzi LP, D'Almeida C, Sampaio G, Castro CC, Sanches MB, Camargo H (2001) Global climatological features in a simulation using the CPTEC-COLA AGCM. J Climate 15:2965–2988

Chang Y, Schubert SD, Suarez MJ (2000) Boreal winter predictions with the GEOS-2 GCM: the role of boundary forcing and initial conditions. Q J R Meteorol Soc 126:2293–2321

Chen WY, Van den Dool HM (1997) Atmospheric predictability of seasonal, annual, and decadal climate means and the role of ENSO cycle: a model study. J Climate 10:1235–1254

Déqué M (1997) Ensemble size for numerical seasonal forecasts. Tellus 49A:74–86

Gan MA, Rao VB (1994) The influence of the Andes Cordillera on transient disturbances. Mon Wea Rev 122:1141–1157

Gates L, Boyle J, Covey C, Dease C, Doutriaux C, Drach R, Fiorino M, Gleckler P, Hnilo J, Marlais S, Phillips T, Potter G, Santer B, Sperber K, Taylor K, Tribbia J (1999) An overview of the results of the atmospheric model intercomparison project (AMIP I). Bull Amer Meteor Soc 80:29–55

Goddard L, Mason SJ, Ropelewski CF, Basher R, Cane MA (2001) Current approaches to seasonal-to-interannual climate predictions. Int J Climatol 21:1111–1152

Gordon HB, O'Farrell SP (1997) Transient Climate change in the CSIRO coupled model with dynamic sea ice. Mon Weather Rev 125:875–907

Grimm AM, Barros VR, Doyle ME (2000) Climate variability in South America associated with El Niño and La Niña events. J Climate 13:35–58

Hurrell JW, Van Loon H, Shea DJ (1998) The mean state of the troposphere. In: Karoly DJ, Vincent DG (eds) Meteorology of the southern hemisphere, meteorological monograph, 27, 49, Amer Meteor Soc pp 1–46

Kalnay E, Kanamitsu M, Kistler R, Collins W, Deaven D, Gandin L, Iredell M, Sha S, White G, Woollen J, Zhu Y, Chelliah M, Ebisuzaki W, Higgins W, Janowiak J, Mo KC, Ropelewski C, Wang J, Leetmaa A, Reynolds R, Roy Jenne, Dennis Joseph (1996) The NCEP/NCAR 40-year Reanalysis Project. Bull Amer Meteor Soc 77(3):437–471

Kiladis GN, Mo KC (1998) Interannual and intraseasonal variability in the Southern Hemisphere. In: Karoly DJ, Vincent DG (eds) Meteorology of the Southern hemisphere, meteorological monograph, 27 (49). Amer Meteor Soc, pp 307–336

Kowalczyk EA, Garratt JR, Krummel PB (1994) Implementation of a soil-canopy scheme into CSIRO GCM. Regional aspects of the model response. CSIRO technical paper No. 32 CSIRO Div. Atmospheric Res., Mordialloc, Australia, 59 pp

Labraga JC, Frumento O (2003) The climate of South America simulated by the coupled model CSIRO Mark 2. Meteorológica 28:63–82

Lacis AA, Hansen JE (1974) A parameterization for the absorption of solar radiation in the earth's atmosphere. J Atmos Sci 31:118–133

Leith CE (1978) Predictability of climate. Nature 276:352–355

Lenters JD, Cook KH (1997) On the origin of the Bolivian high and related circulation features of the South American climate. J Atmos Sci 54:656–677

Marengo JA, Cavalcanti IFA, Satyamurty P, Trosnikov I, Nobre CA, Bonatti JP, Camargo H, Sampaio G, Sanches MB, Manzi AO, Castro CAC, D'Almeida C, Pezzi LP, Candido L (2003) Assessment of regional seasonal rainfall predictability using the CPTEC/COLA atmospheric GCM. Climate Dyn 21(5–6):459–475

McGregor JL (1993) Economical determination of departure points for semi-Lagrangian models. Mon Weather Rev 121:221–230

McGregor JL, Gordon HB, Watterson IG, Dix MR, Rotstayn LD (1993) The CSIRO 9-level atmospheric general circulation model. CSIRO Technical Paper No. 26, CSIRO Div. Atmospheric Res., Mordialloc, Australia, 99 pp

O'Farrell SP (1998) Investigation of the dynamic sea ice component of a coupled atmosphere sea-ice general circulation model. J Geophys Res (Oceans) 103:15751–15782

Peixoto JP, Oort AH (1992) Physics of climate. Am Inst of Phys, College Park, Md, 520 pp

Reynolds WR, Smith TM (1994) Improved global sea surface temperature analyses using optimum interpolation. J Climate 7:929–948

Ropelewski CF, Halpert MS (1987) Global and regional precipitation patterns associated with El Niño/Southern Oscillation. Mon Weather Rev 115:1606–1626

Schwarzkopf MD, Fels SB (1991) The simplified exchange method revisited: an accurate, rapid method for computation of infrared cooling rates and fluxes. J Geophys Res 96:9075–9096

Shukla J, Anderson J, Baumhefner D, Brankovic C, Chang Y, Kalnay E, Marx L, Palmer T, Paolino D, Ploshay J, Schubert S, Straus D, Suarez M, Tribbia J (2000) Dynamical seasonal prediction. Bull Amer Meteor Soc 81(11):2593–2606

Trenberth KE (1997) The definition of El Niño. Bull Amer Meteor Soc 78(12):2771–2777

Watterson IG, Dix MR, Gordon HB, McGregor JL (1995) The CSIRO nine-level atmospheric general circulation model and its equilibrium present and doubled CO_2 climates. Aust Met Mag 44:111–125

Watterson IG, O'Farrell SP, Dix MR (1997) Energy and water transport in climates simulated by a general circulation model that includes dynamic sea ice. J Geophys Res 102:11027–11037

Xie P, Arkin P (1997) Global precipitation: a 17-year monthly analysis based on gauge observations, satellite estimates, and numerical model outputs. Bull Amer Meteor Soc 78:2539–2558

Zhou J, Lau K-M (1998) Does a monsoon climate exist over South America? J Climate 11:1020–1040